Chinese Chemical Letters 34 (2023) 108051

Contents lists available at ScienceDirect

Chinese Chemical Letters

journal homepage: www.elsevier.com/locate/cclet

Enantiomeric hybrid high-temperature multiaxial ferroelectrics with a narrow bandgap and high piezoelectricity

Chang-Feng Wang, Na Wang, Lang Liu*, Le-Ping Miao, Heng-Yun Ye, Yi Zhang, Chao Shi*

Chaotic Matter Science Research Center, Department of Materials, Metallurgy and Chemistry, Jiangxi University of Science and Technology, Ganzhou 341000, China

ARTICLE INFO

Article history:
Received 27 August 2022
Revised 10 November 2022
Accepted 6 December 2022
Available online 8 December 2022

Keywords:
Chirality
Hybrid materials
Multiaxial ferroelectrics
Semiconductors
Piezoelectricity

ABSTRACT

Ferroelectric semiconductors have sparked growing attention in the field of optoelectronics, due to their unique ferroelectric photovoltaic effect. Recently, substantial efforts have been devoted to the development of ferroelectric semiconductors, including inorganic oxides, organic-inorganic hybrids, and metal-free perovskites. Nevertheless, reports of ferroelectric semiconductors with a bandgap of less than 2 eV have been scarce. Here, in combination with the incorporation of triiodide (I_3^-) and the introduction of chiral cations, we successfully constructed a pair of enantiomeric organic-inorganic hybrid ferroelectric semiconductors, (*S*-1,2-DAP·I)$_4$·I_3·BiI_6 and (*R*-1,2-DAP·I)$_4$·I_3·BiI_6 (*R*/*S*-1,2-DAP = (*R*/*S*)-(−)-1,2-diaminopropane), which possess high-temperature multiaxial ferroelectric phase transition with an Aizu notation of 422F2(*s*) at 405 K, a narrow bandgap of 1.56 eV comparable to that of $CH_3NH_3PbI_3$ (~1.5 eV), and an impressive piezoelectric response (piezoelectric coefficient, d_{22} of 35 pC/N) on par with PVDF (polyvinylidene fluoride, 30 pC/N). With intriguing attributes, (*S*-1,2-DAP·I)$_4$·I_3·BiI_6 and (*R*-1,2-DAP·I)$_4$·I_3·BiI_6 exhibit great potential for application of self-power polarized-light detection and piezoelectric sensors.

Ferroelectric semiconductor materials have attracted tremendous attention for their potential applications, such as in information storage, conversion, and self-powered detections [1,2]. Notably, ferroelectric semiconductors possess a photoelectric conversion mechanism different from that of conventional counterparts. Within ferroelectric semiconductors, the internal electric field induced by spontaneous polarization can separate effectively photogenerated charge carriers, which in turn enhances greatly the photophysical properties [3]. The mainstream of ferroelectric semiconductors is currently still dominated by conventional inorganic oxides. However, they suffer from poor light absorption resulting from a wide bandgap, such as $BiFeO_3$ of 2.7 eV, $BaTiO_3$ of 3.2 eV, and $LiNbO_3$ of 3.6 eV, necessitating the development of new narrow bandgap ferroelectric semiconductors [3,4].

Organic-inorganic hybrid halide materials have been demonstrated as excellent semiconductor materials, spearheaded by $CH_3NH_3PbI_3$, due to their desirable optoelectronic performance, such as strong absorption coefficient, long carrier lifetime, and high mobility [5–8]. Moreover, organic-inorganic hybrid halide materials have been proposed as a promising platform for the development of ferroelectric materials due to their structural flexibility and variety [9,10]. Although a mass of hybrid halide ferroelectric semiconductors has been developed with unremitting efforts, most of the reported ones present a wide band gap (> 2 eV) [11–15]. In this context, substantial feasible strategies have been developed to obtain hybrid halide semiconductors with a narrow band gap, such as chemical doping, application of high-pressure, and tailoring perovskite layer thickness [4,16,17]. Among them, chemical doping and high-pressure engineering can efficiently narrow the band gap, but only to a small extent. Excess doping or pressure usually brings about phase transition, in turn losing ferroelectricity, as demonstrated by $(CHA)_2PbBr_{4-4x}I_{4x}$ ($x = 0$–1) [18]. The addition of perovskite layer thickness strategy is limited to two-dimensional (2D) perovskites [19,20]. Recently, iodide management (*i.e.*, incorporation of iodide (I_2) or triiodide (I_3^-) into the crystal lattice) has emerged as a desirable design strategy for the achievement of narrow band gap hybrid semiconductor materials, due to their capacities for decreasing of concentration of deep-level defects and improvement of light absorption, as exemplified by $(C_8H_{11}S)_2Pb_2I_6{}^*I_2$ (1.89 eV), $(Me_3S)_2Pb_5I_{14\times}2I_2$ (1.86 eV), (bis-(2-dimethylaminoethyl)ether)$_3I_3Bi_3I_{14}$ (1.59 eV), (4-methylpiperidinium)$_4$·I_3·BiI_6 (1.58 eV) and (*n*-propylammonium)$_4I_3BiI_6$ (1.34 eV) [21–25]. Despite blooming advances, ferroelectric semiconductor incorporating I_2 or I_3^- still remains a blank. For

* Corresponding authors.
E-mail addresses: amn716@163.com (L. Liu), shic@jxust.edu.cn (C. Shi).

https://doi.org/10.1016/j.cclet.2022.108051
1001-8417/

obtaining ferroelectricity, the introduction of chiral cations is one of the ideal strategies, which has been tested [26]. Because so long as the incorporation of chiral organic cations, according to the chirality transfer principle, the crystal must crystallize in the 11 chiral point groups (1, 2, 222, 4, 422, 3, 32, 6, 622, 23 and 432), five of which (1, 2, 4, 3, 6) allow ferroelectricity [26–28]. It is worth mentioning that chirality-induced ferroelectrics possess a high probability of enjoying a satisfactory piezoelectric response [29,30].

In this work, combined with iodide management and introduction of chirality, we successfully synthesized a pair of hybrid ferroelectric semiconductors, (*R*-1,2-DAP·I)$_4$·I$_3$·BiI$_6$ and (*S*-1,2-DAP·I)$_4$·I$_3$·BiI$_6$ (*R*/*S*-1,2-DAP = (*R*/*S*)-(−)−1,2-diaminopropane), which exhibits a narrow bandgap of 1.56 eV comparable to that of $CH_3NH_3PbI_3$ (∼1.5 eV), a high Curie temperature (T_c) of 405 K, multiaxial feature and high piezoelectric coefficient (d_{22}) of 35 pC/N.

The single crystals of (*S*-1,2-DAP·I)$_4$·I$_3$·BiI$_6$, (*R*-1,2-DAP·I)$_4$·I$_3$·BiI$_6$ and racemic (*Rac*-1,2-DAP·I)$_4$·I$_3$·BiI$_6$ were obtained by evaporation of HI aqueous solution at 323 K (Fig. S1 in Supporting information). The purity of the bulk phases of those compounds was examined by powder X-ray diffraction (PXRD) measurements (Fig. S2 in Supporting information). We carried out the circular dichroism (CD) spectra measurements in the ultraviolet-visible (UV–vis) absorption range to demonstrate the chirality of (*S*-1,2-DAP·I)$_4$·I$_3$·BiI$_6$ and (*R*-1,2-DAP·I)$_4$·I$_3$·BiI$_6$. As depicted in Fig. S3 (Supporting information), (*S*-1,2-DAP·I)$_4$·I$_3$·BiI$_6$ and (*R*-1,2-DAP·I)$_4$·I$_3$·BiI$_6$ exhibit obvious CD signals at the same wavelength, located at around 300, 361, 415, 466 nm, corresponding to those in the UV–vis absorption spectra. The CD signal responses of the (*S*-1,2-DAP·I)$_4$·I$_3$·BiI$_6$ and (*R*-1,2-DAP·I)$_4$·I$_3$·BiI$_6$ are opposite, revealing the enantiomorphic structure feature.

To determine T_c of the (*S*-1,2-DAP·I)$_4$·I$_3$·BiI$_6$ and (*R*-1,2-DAP·I)$_4$·I$_3$·BiI$_6$, we performed differential scanning calorimetry (DSC) measurements, which is an overwhelmingly reliable method to detect the T_c of the molecular ferroelectrics [31–33]. The results of (*S*-1,2-DAP·I)$_4$·I$_3$·BiI$_6$ and (*R*-1,2-DAP·I)$_4$·I$_3$·BiI$_6$ are the same (Figs. S4 and S5a in Supporting information). As shown in Fig. S4, an anomalous endothermic peak appears at around 405 K in the heating run, and the corresponding exothermic peak is determined at around 394 K in the cooling run, indicating that (*S*-1,2-DAP·I)$_4$·I$_3$·BiI$_6$ undergoes a reversible phase transition. The large thermal hysteresis (11 K) suggests that the phase transition belongs to the first-order ones [34,35]. The phase above and below the T_c is labeled as the high-temperature phase (HTP) and low-temperature phase (LTP), respectively. The enthalpy change (ΔH) and entropy change (ΔS) in the phase transition process are determined as 9.47 J/g and 50 J mol^{-1} K^{-1}, respectively. In light of the Boltzmann equation, $\Delta S = R\ln N$, in which R is the gas constant (8.314), and N is the ratio of the numbers of respective geometrically distinguishable orientations, the calculated N value is about 418, disclosing that the phase transition of (*S*-1,2-DAP·I)$_4$·I$_3$·BiI$_6$ can be classified as the ordered-disordered ones, and the HTP is highly disordered. Significantly, T_c (405 K) of (*S*-1,2-DAP·I)$_4$·I$_3$·BiI$_6$ is higher than that of $BaTiO_3$ (393 K) and those of recently reported ferroelectrics, such as (4,4-difluorocyclohexylammonium)$_2$PbI$_4$, [(*S*/*R*)-N-(1-phenylethyl)ethane-1,2-diaminium]PbI$_4$ and (*n*-propylammonium)$_2$CsAgBiBr$_7$ [15,36,37]. Similarly, (*Rac*-1,2-DAP·I)$_4$·I$_3$·BiI$_6$ also exhibits high-temperature reversible phase transitions at 448 K (Fig. S5b in Supporting information).

We take (*S*-1,2-DAP·I)$_4$·I$_3$·BiI$_6$ as an example to analyze structure in the LTP and HTP because (*S*-1,2-DAP·I)$_4$·I$_3$·BiI$_6$ and (*R*-1,2-DAP·I)$_4$·I$_3$·BiI$_6$ are enantiomorphic each other. To disclose the mechanism of paraelectric-ferroelectric phase transition for (*S*-1,2-DAP·I)$_4$·I$_3$·BiI$_6$, we performed the variable-temperature single-crystal X-ray diffraction measurements. Racemic (*Rac*-1,2-DAP·I)$_4$·I$_3$·BiI$_6$ adopts a centrosymmetric space group of $P2_1/c$ (point group of $2/m$). In the LTP (ferroelectric phase), (*S*-1,2-DAP·I)$_4$·I$_3$·BiI$_6$ adopts a 0D structure, and crystallizes in the monoclinic space group of $P2_1$ (point group of 2) with a cell parameter: $a = 14.2307(4)$ Å, $b = 14.1214(3)$ Å, $c = 24.3679(6)$ Å, $\beta = 105.702(3)^\circ$ and $V = 4714.17$ Å^3 (Table S1 in Supporting information). The asymmetric unit is composed of eight different geometry configurations *S*-1,2-DAP cations, two I_3^- anions, eight free I^- anions and two discrete BiI_6^{3-} octahedral. As shown in Fig. 1a, the structure of (*S*-1,2-DAP·I)$_4$·I$_3$·BiI$_6$ can be regarded as a sandwich structure, which consists of organic cation layers, I^- anion ones and ones composed of alternating I_3^- anions, and discrete BiI_6^{3-} octahedral. By weak N–H···I and C–H···I hydrogen bonds, *S*-1,2-DAP cations act as bridging linkers to bond the I^- anion layers and layers composed of I_3^- anions and BiI_6^{3-} octahedral (Fig. 1b). Polar structure brings about spontaneous polarization (P_s) along the [010]-direction, *i.e.*, *b*-axis.

In the HTP, (paraelectric phase), The space group changes to tetragonal group space of $I4_122$ (point group of 422) with a cell parameter: $a = 10.1224(6)$ Å, $c = 47.470(3)$ Å, and $V = 4863.92$ Å^3 (Table S1). As depicted in Fig. 1c, BiI_6^{3-} octahedral become more geometrically regular, and the organic cations become disordered around the crystallographic C_2 rotation axis parallel to the *c*-axis (Fig. 1d). The relationship of cell parameters between the HTP and LTP can be described to be $b^{LTP} \approx a^{HTP} + b^{HTP}$, $a^{LTP} \approx b^{HTP} - a^{HTP}$ and $c^{LTP} \approx 1/2a^{HTP} + 1/2c^{HTP} - 1/2b^{HTP}$ (Fig. 1e). Since the crystallographic symmetry changes from the point group of 422 (E, $2C_4$, C_2, $2C'_2$, $2C''_2$) to 2 (E, C_2), (*R*-1,2-DAP·I)$_4$·I$_3$·BiI$_6$ and (*S*-1,2-DAP·I)$_4$·I$_3$·BiI$_6$ belong to the ferroelectric species with Aizu nation 422F2(*s*) [31]. In view of the change in the number of symmetry element, the ferroelectric phase possesses four equivalent polarization directions, *i.e.*, (*R*-1,2-DAP·I)$_4$·I$_3$·BiI$_6$ and (*S*-1,2-DAP·I)$_4$·I$_3$·BiI$_6$ are of multiaxial ferroelectrics (Fig. 1e).

To confirm the paraelectric-ferroelectric phase transition of (*S*-1,2-DAP·I)$_4$·I$_3$·BiI$_6$ and (*R*-1,2-DAP·I)$_4$·I$_3$·BiI$_6$, we measured the second harmonic generation (SHG) signal as a function of temperature. As shown in Fig. 2a, in the LTP, the SHG signal response of (*S*-1,2-DAP·I)$_4$·I$_3$·BiI$_6$ exhibits an active state, which is in line with the polar point group of 2. As the temperature rises to around T_c, the SHG signal intensity drops sharply, and decreases to zero above T_c. Chiral point group of 422 are not SHG-active, due to restriction of Kleinman symmetry [32,33]. This variable-temperature SHG signal response agrees with the paraelectric-ferroelectric phase transition for the 422F2(*s*) type.

Usually, paraelectric-ferroelectric phase transitions are characterized by the anomalies of dielectric permittivity ($\varepsilon = \varepsilon' - i\varepsilon''$, in which ε' and ε'' represent the real and the imaginary parts in several) at around T_c [34,35]. Then, we measured variable-temperature ε' of the (*S*-1,2-DAP·I)$_4$·I$_3$·BiI$_6$ at 1 MHz. As shown in Fig. 2b, the steplike anomaly of ε' is observed at around 405 and 394 K in the heating and cooling run, respectively, corresponding to the DSC results, indicating that there is a reversible phase transition.

To confirm the polarization reversal in (*S*-1,2-DAP·I)$_4$·I$_3$·BiI$_6$, we measured the polarization-electric ($P-E$) field hysteresis loop along the *b*-axis direction on a single-crystal slice at 333 K with the double-wave method at frequency of 50 Hz (The detailed process for determination of the *b*-axis direction can be seen in Supporting information). Notably, the measurements were carried out at relatively high temperature to facilitate reversal of P_s, which is common for molecule-based ferroelectrics [36]. As shown in Fig. 2c, the obtained current density-electric field (J–E) loop exhibits two opposite peaks in the different directions of the electric field. Such J–E response is due to the polarization reversal upon the electric field exceeding a particular value, known as the coercive field (E_c). The P–E loop calculated from the J–E loop possesses a high rectangularity, which unambiguously proves ferroelectricity of (*S*-1,2-DAP·I)$_4$·I$_3$·BiI$_6$ (Fig. 2c). The P_s and E_c are determined to be 1.62 μC/cm^2 and 11 kV/cm, respectively. The P_s of (*S*-1,2-DAP·I)$_4$·I$_3$·BiI$_6$

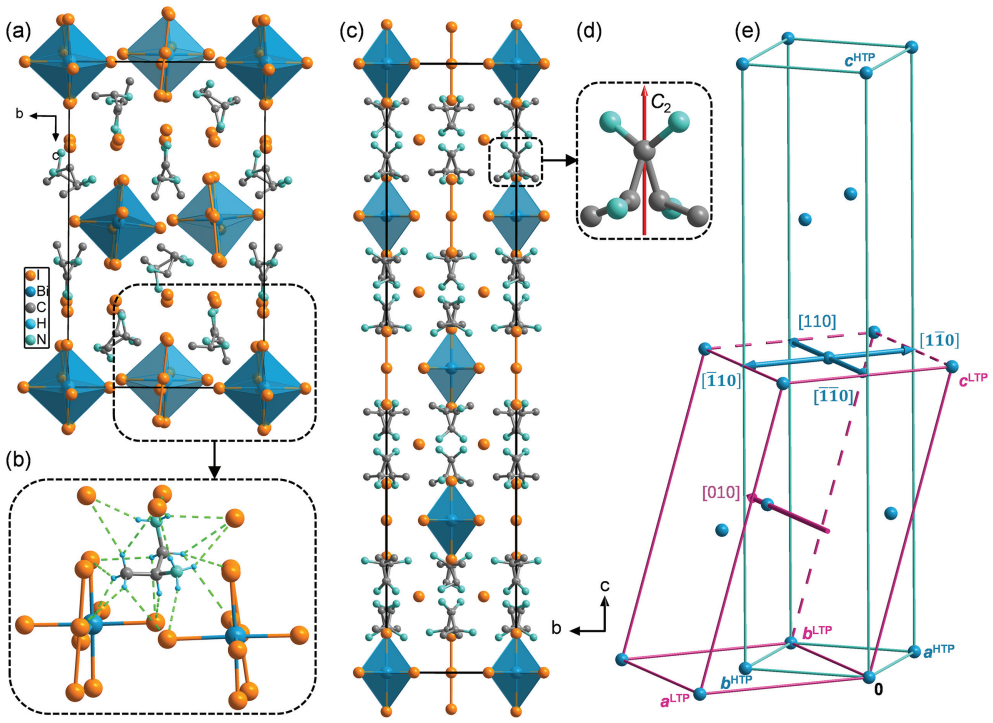

Fig. 1. The packing structure of (*S*-1,2-DAP·I)$_4$·I$_3$·BiI$_6$ in the LTP (a) and HTP (c) (H atoms are omitted for clarity). (b) Distribution of hydrogen bonds of *S*-1,2-DAP cations. (d) Two-fold disordered *S*-1,2-DAP cations around C_2 rotation axis in the HTP. (e) The relationship of the unit cells of (*S*-1,2-DAP·I)$_4$·I$_3$·BiI$_6$ between the LTP and HTP. The red and blue edges represent the crystal lattice of the LTP and the HTP, respectively. The red arrow represents the spontaneous polarization direction in the LTP. The blue arrows represent the possible equivalent polarization directions. Only the Bi atoms are shown for clarity.

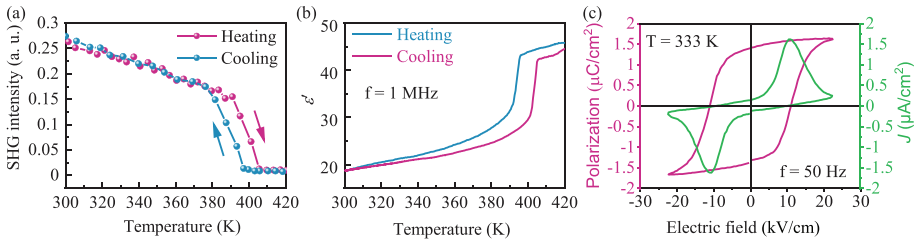

Fig. 2. The ferroelectricity and related properties of (*S*-1,2-DAP·I)$_4$·I$_3$·BiI$_6$. (a) The SHG signal intensity a function of temperature. (b) The ε' in the different temperature at 1 MHz. (c) The $P-E$ hysteresis loop at 333 K.

is greater than those recently reported ferroelectrics, such as [(2-aminoethyl)trimethylphosphanium)]$_2$PbBr$_4$ (0.95 μC/cm^2), and (4,4-difluorohexahydroazepine)$_2$PbI$_4$ (1.1 μC/cm^2), but is smaller than those of (4,4-difluoropiperidinium)$_2$PbI$_4$ (10 μC/cm^2), (4-(aminomethyl)piperidinium)PbI$_4$ (9.8 μC/cm^2), (*S*)−3-F-(pyrrolidinium)CdCl$_3$ (5.79 μC/cm^2), (*R*)−3-F-(pyrrolidinium)CdCl$_3$ (5.63 μC/cm^2), (isoamylammonium)$_2$(methylammonium)$_2$Pb$_3$Br$_{10}$ (5 μC/cm^2), (C$_4$H$_9$NH$_3$)$_2$CsPb$_2$Br$_7$ (4.2 μC/cm^2), and (C$_4$H$_9$NH$_3$)$_2$PbCl$_4$ (2.1 μC/cm^2) [14,37-43]. (*R*-1,2-DAP·I)$_4$·I$_3$·BiI$_6$ possess similar ferroelectricity and related properties (Fig. S6 in Supporting information).

In a ferroelectric crystal, there are equivalent directions of P_s, and the probability of occurrence of these polarization directions is equal. Therefore, a ferroelectric crystal usually shows a multi-domain structure, which minimizes the energy of the system. Piezoresponse force microscopy (PFM) has been fully proven to be a useful tool for characterizing the domain structure of ferroelectrics at the nanoscale. Vertical and lateral PFM imaging can detect the out-of-plane and in-plane components of polarization, respectively [44]. Each PFM component consists of amplitude and phase signal, which reflect the intensity of piezoelectric response and direction of polarization, respectively. We simultaneously measured the lateral and vertical PFM on a bulk single crystal in the same area (5 × 5 μm^2) at room temperature. As depicted in Figs. 3a-e, the observed domains with irregular shapes are irrelevant to the topography, indicating that the signal originates from the polarization state rather than from the interference in topography. For the lateral PFM, the amplitude patterns (Fig. 3a) agree with phase patterns (Fig. 3b), in which domain walls with weak piezoelectric responses separate the domains with strong piezoelectric responses. However, the domain structures of vertical PFM are different from lateral PFM (Figs. 3d and e), implying that there is the existence of non-180° domains [45]. Hence, (*S*-1,2-DAP·I)$_4$·I$_3$·BiI$_6$ should belong to the multiaxial ferroelectrics, which is consistent with the structural analysis. To confirm (*S*-1,2-DAP·I)$_4$·I$_3$·BiI$_6$ possesses the switchable P_s, we measured switching spectroscopy lateral PFM at a selected point. The phase-bias loop (red line) and amplitude-bias loop (blue line) were recorded in Fig. 3f. When the

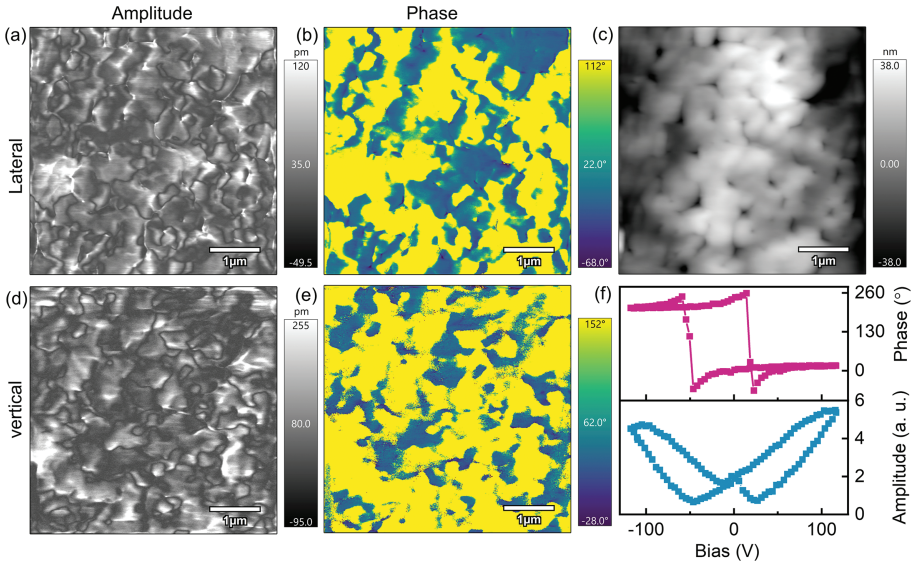

Fig. 3. The PFM measurement results of (*S*-1,2-DAP·I)$_4$·I$_3$·BiI$_6$. The lateral PFM (a) amplitude and (b) phase images. (c) The topographical image. The vertical PFM (d) amplitude and (e) phase images. (f) The signal of the lateral PFM phase (red line) and amplitude (blue line) as functions of tip DC bias voltage at a selected point.

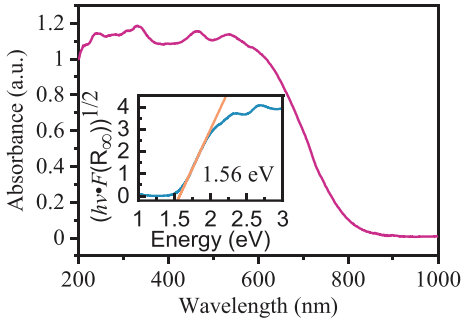

Fig. 4. The UV–vis absorbance spectrum of (*S*-1,2-DAP·I)$_4$·I$_3$·BiI$_6$. The inset shows the *Tauc* plot for fitting the indirect band gap of 1.56 eV.

applied bias voltage exceeds the coercive voltage, the phase is reversed, demonstrating that the P_s is switchable. The polarization switching behavior with hysteresis gives rise to the amplitude-bias butterfly-like loop. Furthermore, measurements of ferroelectric domains switching for (*S*-1,2-DAP·I)$_4$·I$_3$·BiI$_6$ were carried out. As shown in Fig. S7a (Supporting information), applying $a+45$ V voltage pulse with a duration of 5 s on a selected point (marked by green), the polarization direction appears the reverse (Fig. S7b in Supporting information), confirming its ferroelectricity.

The *quasi*-static method was employed to measure the piezoelectric coefficient (d_{22}) on the single-crystal of (*S*-1,2-DAP·I)$_4$·I$_3$·BiI$_6$ along the *b*-axis at room temperature [46]. As shown in Fig. S8 (Supporting information), the d_{22} of (*S*-1,2-DAP·I)$_4$·I$_3$·BiI$_6$ was determined to be about 35 pC/N, which is greater than those of $LiNbO_3$ (11 pC/N), MDABCO–NH_4I_3 (14 pC/N), and TGS (triglycine sulfate, 22 pC/N), comparable to that for PVDF (polyvinylidene fluoride, 30 pC/N), but is smaller than those of (4-aminotetrahydropyran)$_2PbBr_4$ (76 pC/N), [$(CH_3)4N$][$FeCl_4$] (80 pC/N), (TMBM)$MnBr_3$ (112 pC/N), (TMCM)$CdBr_3$ (139 pC/N), and (TMCM)$MnCl_3$ (185 pC/N) [36,47].

To evaluate the bandgap of (*S*-1,2-DAP·I)$_4$·I$_3$·BiI$_6$ and (*R*-1,2-DAP·I)$_4$·I$_3$·BiI$_6$, the UV–vis absorption spectrum was recorded at room temperature. As shown in Fig. 4, the (*S*-1,2-DAP·I)$_4$·I$_3$·BiI$_6$ possesses a gradually decreasing absorption edge in the range from 540 nm to 840 nm, implying an indirect bandgap. Using the *Tauc* equation (for details process see Supporting information), the value of bandgap was determined to be about 1.56 eV (inset of Fig. 4), which is an abnormally narrow bandgap among reported ferroelectric semiconductors, and even almost comparable to $CH_3NH_3PbI_3$ (~1.5 eV) (Fig. S9 in Supporting information). (*R*-1,2-DAP·I)$_4$·I$_3$·BiI$_6$ also possesses the same bandgap, 1.56 eV, (Fig. S10 in Supporting information). The narrow bandgap of (*S*-1,2-DAP·I)$_4$·I$_3$·BiI$_6$ and (*R*-1,2-DAP·I)$_4$·I$_3$·BiI$_6$ is ascribed to the introduction of I_3^- ions, as reported by the previous reports [21–25]. I-5p orbitals of I_3^- ions lower the bottom of the conduction band.

In summary, we have developed a pair of chiral hybrid compounds, (*R*-1,2-DAP·I)$_4$·I$_3$·BiI$_6$ and (*S*-1,2-DAP·I)$_4$·I$_3$·BiI$_6$. Benefited from intercalation of I_3^- ions, (*R*-1,2-DAP·I)$_4$·I$_3$·BiI$_6$ and (*S*-1,2-DAP·I)$_4$·I$_3$·BiI$_6$ exhibit a narrow bandgap of 1.56 eV comparable to that of $CH_3NH_3PbI_3$, which is confirmed by UV–vis absorbance spectrum. Moreover, by the introduction of chirality, (*R*-1,2-DAP·I)$_4$·I$_3$·BiI$_6$ and (*S*-1,2-DAP·I)$_4$·I$_3$·BiI$_6$, possess multiaxial ferroelectricity and efficient piezoelectric response of 35 pC/N. This work provides inspiration for the direct design of molecular ferroelectric with the desired function.

Declaration of competing interest

The authors declare that they have no known competing financial interests or personal relationships that could have appeared to influence the work reported in this paper.

Acknowledgments

This work was supported financially by the National Key Research and Development Program of China (No. 2017YFA0204800), National Natural Science Foundation of China (Nos. 22175079 and 21875093), Natural Science Foundation of Jiangxi Province (Nos. 20204BCJ22015 and 20202ACBL203001), Jiangxi Provincial Department of Education Science and Technology Research Project (No. GJJ210812), Jiangxi Provincial Natural Science Foundation of China (No. 20212BAB214021), Science and Technology Project of Jiangxi Provincial Department of Education (No. GJJ200836).

Supplementary materials

Supplementary material associated with this article can be found, in the online version, at doi:10.1016/j.cclet.2022.108051.

References

[1] Y.Y. Tang, P.F. Li, W.Q. Liao, et al., J. Am. Chem. Soc. 140 (2018) 8051–8059.
[2] Z. Wu, W. Zhang, H. Ye, et al., J. Am. Chem. Soc. 143 (2021) 7593–7598.
[3] I. Grinberg, D.V. West, M. Torres, et al., Nature 503 (2013) 509–512.
[4] S. Han, M. Li, Y. Liu, et al., Nat. Commun. 12 (2021) 284.
[5] X. Li, J.M. Hoffman, M.G. Kanatzidis, Chem. Rev. 121 (2021) 2230–2291.
[6] S. Liu, L. He, Y. Wang, et al., Chin. Chem. Lett. 33 (2022) 1032–1036.
[7] Q. Jia, T. Shao, L. Tong, et al., Chin. Chem. Lett. 34 (2023) 107539.
[8] C. Su, Z. Zhang, J. Yao, et al., Chin. Chem. Lett. 34 (2023) 107442.
[9] C.F. Wang, H. Li, Q. Ji, et al., Adv. Funct. Mater. 32 (2022) 2205918.
[10] L. Mao, C.C. Stoumpos, M.G. Kanatzidis, J. Am. Chem. Soc. 141 (2018) 1171–1190.
[11] C. Ji, D. Dey, Y. Peng, et al., Angew. Chem. Int. Ed. 59 (2020) 18933–18937.
[12] L. Li, X. Liu, C. He, et al., J. Am. Chem. Soc. 142 (2020) 1159–1163.
[13] W. Zhang, M. Hong, J. Luo, J. Am. Chem. Soc. 143 (2021) 16758–16767.
[14] H.Y. Zhang, Z.X. Zhang, X.G. Chen, et al., J. Am. Chem. Soc. 143 (2021) 1664–1672.
[15] Y.L. Zeng, X.Q. Huang, C.R. Huang, et al., Angew. Chem. Int. Ed. 60 (2021) 10730–10735.
[16] G. Liu, L. Kong, J. Gong, et al., Adv. Funct. Mater. 27 (2016) 1604208.
[17] Y.Y. Chen, C.H. Gao, T. Yang, et al., Chin. J. Struct. Chem. 41 (2022) 2204001–22040011.
[18] H.Y. Ye, W.Q. Liao, C.L. Hu, et al., Adv. Mater. 28 (2016) 2579–2586.
[19] L. Li, X. Liu, Y. Li, et al., J. Am. Chem. Soc. 141 (2019) 2623–2629.
[20] L. Li, Z. Sun, P. Wang, et al., Angew. Chem. Int. Ed. 56 (2017) 12150–12154.
[21] A. Starkholm, L. Kloo, P.H. Svensson, ACS Appl. Energy Mater. 2 (2018) 477–485.
[22] B. Kou, W. Zhang, C. Ji, et al., Chem. Commun. 55 (2019) 14174–14177.
[23] W. Zhang, B. Kou, Y. Peng, et al., J. Mater. Chem. C 6 (2018) 12170–12174.
[24] W. Zhang, X. Liu, L. Li, et al., Chem. Mater. 30 (2018) 4081–4088.
[25] W.S. Yang, B.W. Park, E.H. Jung, et al., Science 356 (2017) 1376–1379.
[26] H.Y. Zhang, Y.Y. Tang, P.P. Shi, et al., Acc. Chem. Res. 52 (2019) 1928–1938.
[27] V. Mujica, Nat. Chem. 7 (2015) 543–544.
[28] G. Long, R. Sabatini, M.I. Saidaminov, et al., Nat. Rev. Mater. 5 (2020) 423–439.
[29] C.F. Wang, C. Shi, A. Zheng, et al., Mater. Horiz. 9 (2022) 2450–2459.
[30] C. Shi, J.J. Ma, J.Y. Jiang, et al., J. Am. Chem. Soc. 142 (2020) 9634–9641.
[31] K. Aizu, Phys. Rev. 146 (1966) 423–429.
[32] D.A. Kleinman, Phys. Rev. 126 (1962) 1977–1979.
[33] Y. Xue, Z. Zhang, P. Shi, et al., Chin. Chem. Lett. 32 (2021) 539–542.
[34] W.P. Zhao, C. Shi, A. Stroppa, et al., Inorg. Chem. 55 (2016) 10337–10342.
[35] M.E. Kamminga, A. Stroppa, S. Picozzi, et al., Inorg. Chem. 56 (2017) 33–41.
[36] Y.M. You, W.Q. Liao, D. Zhao, et al., Science 357 (2017) 306–309.
[37] T.T. Sha, Y.A. Xiong, Q. Pan, et al., Adv. Mater. 31 (2019) 1901843.
[38] H.Y. Zhang, X.J. Song, X.G. Chen, et al., J. Am. Chem. Soc. 142 (2020) 4925–4931.
[39] I.H. Park, Q. Zhang, K.C. Kwon, et al., J. Am. Chem. Soc. 141 (2019) 15972–15976.
[40] Y.Y. Tang, Y. Ai, W.Q. Liao, et al., Adv. Mater. 31 (2019) 1902163.
[41] M. Li, Y. Xu, S. Han, et al., Adv. Mater. 32 (2020) 2002972.
[42] Z. Wu, C. Ji, L. Li, et al., Angew. Chem. Int. Ed. 57 (2018) 8140–8143.
[43] C. Ji, S. Wang, L. Li, et al., Adv. Funct. Mater. 29 (2019) 1805038.
[44] H. Lu, T. Li, S. Poddar, et al., Adv. Mater. 27 (2015) 7832–7838.
[45] X.G. Chen, X.J. Song, Z.X. Zhang, et al., J. Am. Chem. Soc. 142 (2020) 10212–10218.
[46] H.Y. Ye, Y.Y. Tang, P.F. Li, et al., Science 361 (2018) 151–155.
[47] Q. Pan, Y.A. Xiong, T.T. Sha, et al., Mater. Chem. Front. 5 (2021) 44–59.